J Mater Sci (2010) 45:6685–6693
DOI 10.1007/s10853-010-4761-4

Effects of sintering temperature on the microstructure and dielectric properties of titanium dioxide ceramics

Sheng Chao · Vladimir Petrovsky · Fatih Dogan

Received: 22 April 2010 / Accepted: 9 July 2010 / Published online: 21 July 2010

Abstract Nanostructured (~200 nm grain size) titanium dioxide (TiO_2) ceramics were densified at temperature as low as 800 °C by pressureless sintering in a pure oxygen atmosphere. Phase transition and microstructural development of sintered samples were studied by X-ray diffraction (XRD) and scanning electron microscopy (SEM). Dielectric properties including d.c. conductivity, dielectric constant, loss tangent, and dielectric breakdown strength (BDS) were determined for samples sintered at various temperatures. The influence of sintering temperature on the microstructural development, defect chemistry, and dielectric properties of TiO_2 is discussed. Nanostructured TiO_2 ceramics with high sintering density (>98%) lead to improved dielectric properties; high BDS (~1800 kV/cm), low electrical conductivity (~5×10^{-15} S/cm), high dielectric constant (~130), and low loss tangent (~0.09% at 1 kHz), which is promising for application in high energy density capacitors.

Introduction

TiO_2 is one of the most widely used metal oxides, which has broad range of applications, including pigments, gas and humidity sensors, catalyst support, solar cells, and capacitors [1–6]. As a dielectric material, TiO_2 combines the merit of both relatively high dielectric constant (>100) [7] and high breakdown strength (BDS, >1000 kV/cm) [8] which are two important parameters to fabricate capacitors with high energy density. For ideal (assuming no dielectric loss) linear dielectrics the volumetric energy density (W, J/m^3) is governed by the following equation:

$$W_{(\text{vol.})} = \frac{1}{2}\varepsilon_0\varepsilon_r E_b^2 \quad (1)$$

where ε_0 is the permittivity of vacuum (8.854×10^{-12} F/m), ε_r is the relative permittivity (dielectric constant) of the dielectric material, and E_b (V/m) is the BDS of the dielectric material.

Although TiO_2 has been widely studied with respect to synthesis of nanosized powders [9, 10], thin film fabrication [11, 12], and sintering of nanostructured TiO_2 ceramics [13–15], little attention has been paid on dielectric properties of nanostructured bulk TiO_2 ceramics. It is well known that the properties of electroceramics are affected by their microstructural features (such as grain size, porosity, secondary phases) and defect structure (such as point and electronic defects). The objective of this study is to investigate the effect of sintering conditions on the microstructural development and dielectric properties of TiO_2 ceramics for potential application in high energy density capacitor.

Experimental

Sintering studies of TiO_2 were conducted using nanosized TiO_2 powders (Nanophase Technologies Corporation Romeoville, IL). Powder characteristics and main impurities (from the product data sheet) are shown in Tables 1 and 2, respectively. Green compacts were prepared by uniaxial pressing of powders (without binder) at ~100 MPa followed by cold isostatic pressing at ~300 MPa . Sintering of the samples was conducted at various temperatures (700–1000 °C) in pure oxygen

S. Chao · V. Petrovsky · F. Dogan (✉)
Department of Materials Science and Engineering, Missouri University of Science and Technology, Rolla, MO 65409, USA
e-mail: doganf@mst.edu

Table 1 TiO_2 powder characteristics

Characteristics	Value
Purity (%)	99.9
Average particle size (nm)	40
Specific surface area (m^2/g)	38
Bulk density (g/cm^3)	0.20
True density (g/cm^3)	3.95
Crystal phase	80% anatase and 20% rutile

Table 2 Main impurities in the TiO_2 powder

Elements	Impurity level (wt%)
Fe	0.037
Mg	0.032
Ca	0.024
Al	0.0089

(1 atm.) for 12 h with a heating and cooling rate of 4 and 5 °C/min, respectively. Sintered densities were determined by Archimedes' method using water as immersion liquid and assuming theoretical densities of anatase 3.89 g/cm^3 and rutile 4.25 g/cm^3 [14]. Phase evolution of the samples at various temperatures was determined by X-ray diffraction (XRD) (Philips X'Pert, Holand). Microstructural development of as-fired fracture surfaces was observed by scanning electron microscopy (SEM) (Hitachi S4700, Japan). Grain size of the samples was determined by linear intercept method by counting of at least 100 grains from SEM images of the microstructure.

For electrical measurements, the samples (~10 mm diameter and ~0.8 mm thickness) were polished using 5 μm diamond suspension and electroded with silver paste as top and bottom electrodes. Electrical properties were measured in a temperature controllable Delta 9023 environmental chamber (Delta Design, Inc. San Diego, CA, USA) in air. D.C. conductivity measurements were performed using a Keithley 6517 Electrometer (Keithley Instruments, Cleveland, USA). Dielectric constant of the samples was calculated according to the capacitance measured with a Solartron 1260 impedance analyzer connected with a Solartron 1296 dielectric interface (Solartron analytical, Hampshire, England) in the frequency range of 1 Hz to 1 MHz and voltage amplitude of 1 V. Polarization as a function of electrical field was measured with a ferroelectric tester (RT6000, Radiant Technology, NM, USA). For BDS measurements, d.c. voltage was supplied by a Spellman SL30 high voltage generator (Spellman high voltage electronics corporation, New York, USA), with a fixed ramp rate of 250 V/s. A dimpled electrode configuration was employed for BDS measurements to ensure that maximum electrical stress is concentrated at the thinnest point (~80–100 μm) of the sample. This sample configuration allowed to measure intrinsic BDS of the samples by eliminating of electrical field enhancement at the electrode edges [16]. A more detailed description of sample preparation and BDS measurements is given elsewhere [17].

Results and discussion

Microstructural development

Relative densities of TiO_2 ceramics sintered at various temperatures are shown in Fig. 1. A sintering density (relative density with respect to the theoretical density) of 97.3% was obtained at 780 °C, further increase of the sintering temperature up to 1000 °C lead to nearly full densification of the samples. Although TiO_2 nanopowders have been densified at even lower temperatures (700 °C by spark plasma sintering [18] or 400 °C by hot-pressing at very high pressures [14]), highly dense TiO_2 ceramics were obtained by conventional pressureless sintering at 800 °C in the present study. Enhanced sintering of the samples is attributed to nanosized starting powders and well-compacted (~60% packing density) green pellets after isostatic pressing. As shown in Table 3, a high green density led to a high sintering density as it applies for densification of most ceramic materials.

Figure 2 shows the microstructure of TiO_2 ceramics with a grain size ranging from ~0.15 μm for samples sintered at 700 °C to ~2.70 μm after sintering at 1000 °C. Residual porosity is observed in samples sintered at temperatures below 800 °C (Fig. 2e) in accordance with the density measurements. The samples sintered at lower

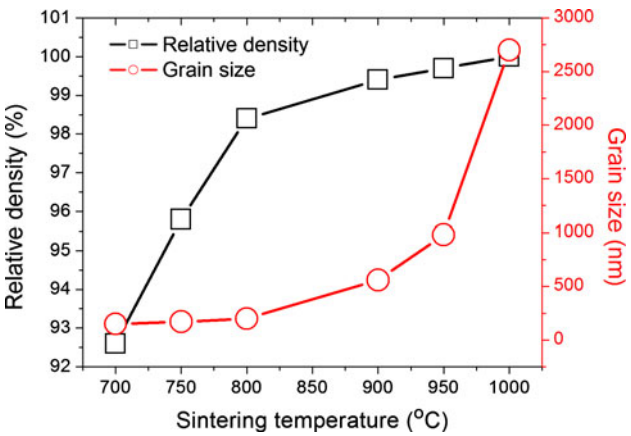

Fig. 1 Relative density and grain size of TiO_2 ceramics as a function of sintering temperature

Table 3 Relationship between green compact density and sintering density

Green density (%)	Relative density after sintering at 800 °C (%)
36	82.3
41	89.3
48	96.2
60	98.3

temperatures revealed a uniform grain size, whereas a bimodal grain size distribution was observed in samples sintered at higher temperatures, indicating that the grain growth occurred according to Ostwald-ripening mechanism.

Figure 3 shows XRD patterns of TiO_2 samples sintered at various temperatures. Weak intensity peaks corresponding to the remaining anatase phase (JCPDS 73-1764) were identified in the sample sintered at 700 °C while samples sintered at temperatures equal to or higher than 750 °C showed the rutile phase (JCPDS 21-1276). The temperature

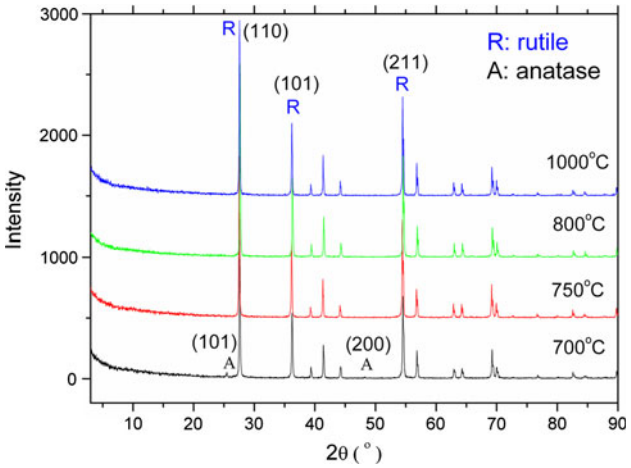

Fig. 3 XRD patterns of TiO_2 samples sintered at various temperatures (all peaks were indexed to rutile or anatase phase)

of anatase to rutile phase transformation is reported to be ~915 °C [19]. In the present study, greatly reduced phase transition temperature is attributed to nanosized starting powders with high specific surface area. Similar results

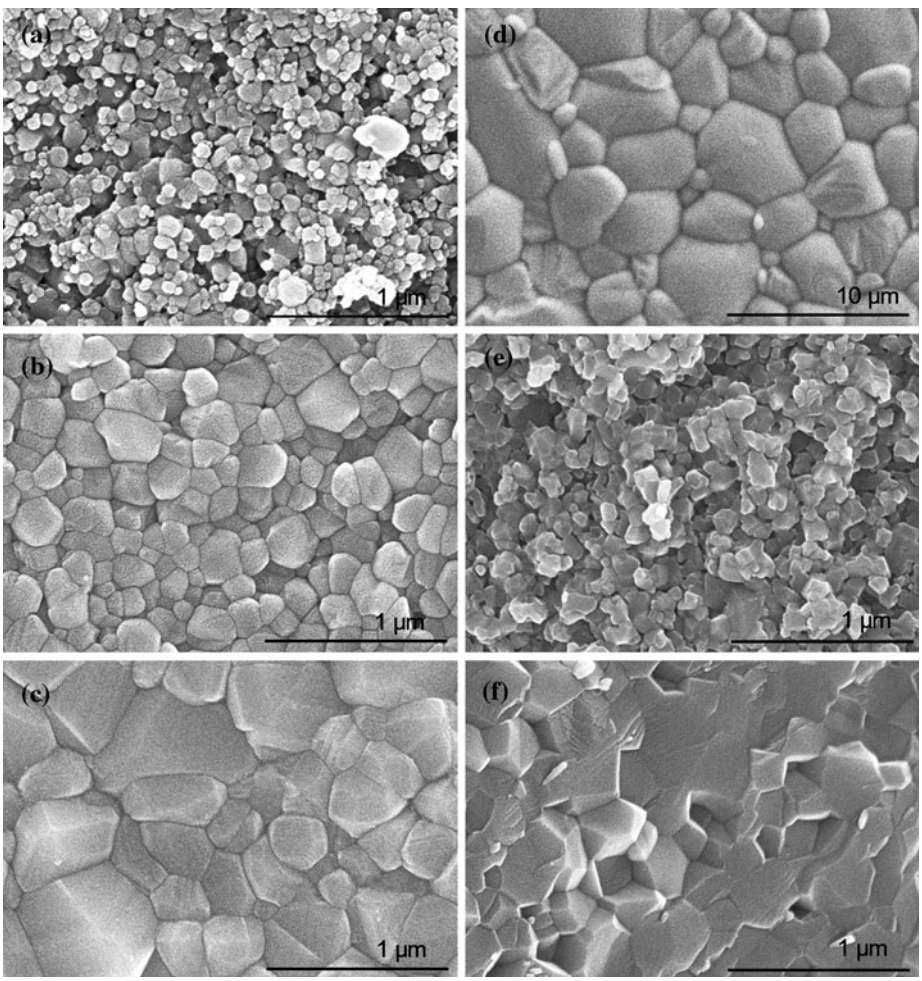

Fig. 2 Microstructural development of TiO_2 ceramics sintered at **a** 700 °C, **b** 800 °C, **c** 900 °C, **d** 1000 °C, **e** 700 °C (fracture surface), **f** 800 °C (fracture surface)

were obtained in a study by Eastman [20] that reported the completion of anatase to rutile transformation of TiO_2 nanosized powders between 650 and 800 °C.

Dielectric properties

Dielectric properties were measured on selected samples sintered at 700, 800, 900, and 1000 °C (named as T7, T8, T9, and T10, respectively afterwards). The frequency dependence of dielectric constant and loss tangent of these samples measured at room temperature are shown in Fig. 4. While the dielectric constant of sample T7 decreased from 133 at 1 Hz to 113 at 100 kHz, a more stable frequency dependent dielectric constant was observed in case of sample T8. In the frequency range from 1 Hz to 100 kHz, dielectric constant of sample T8 decreased slightly from 134 to 133. Relatively large variation in dielectric constant of sample T7 is attributed to high d.c. conductivity that led to high apparent dielectric constant and high loss tangent at low frequencies. Because of the lower sintering density of sample T7, the intrinsic dielectric constant measured at high frequency (100 kHz) was ~15% lower than that of sample T8.

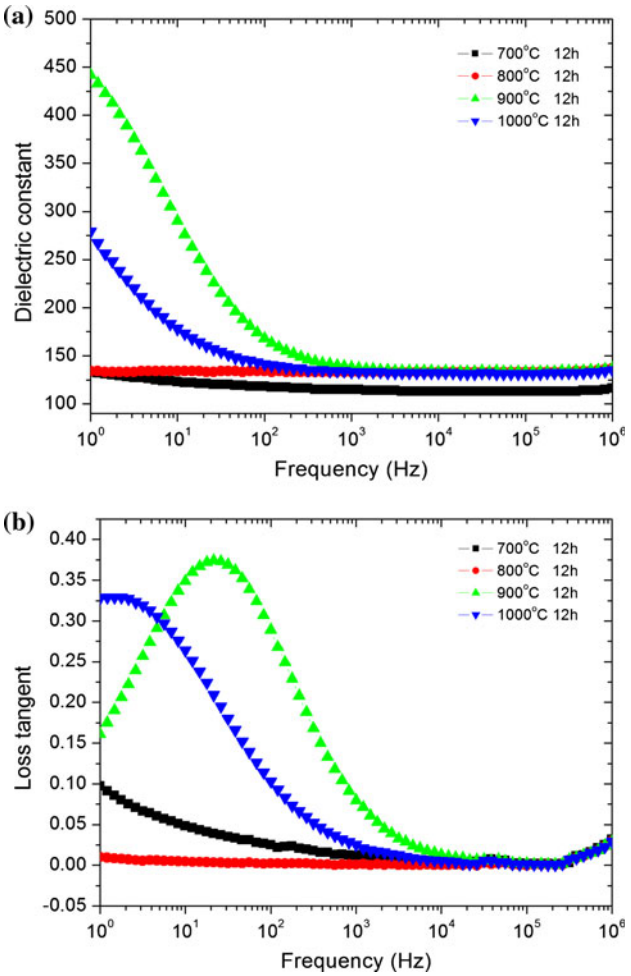

Fig. 4 **a** Dielectric constant and **b** loss tangent of TiO_2 samples sintered at various temperatures

Unlike low temperature sintered samples (T7 and T8), the dielectric constant of sample T9 and T10 was found to have a strong dependence on the measuring frequencies. At low frequencies (1 Hz–1 kHz), the dielectric constant of T9 and T10 exceeded the intrinsic dielectric constant of randomly orientated polycrystalline TiO_2 ceramics [21]. With increasing frequency, the dielectric constant gradually decreased and finally reached a plateau with K: ~133, matching the dielectric constant of sample T8. High dielectric constant at low frequencies may arise from a polarization mechanism other than electronic and ionic polarizations. As the external stimulus frequency increases, this polarization mechanism gradually lag behind and damp out, resulting in a decrease of the dielectric constant as the frequency increases.

As shown in Fig. 4b, accompanied with this dielectric constant anomaly, a pronounced loss tangent peak was observed for samples sintered at higher temperatures (T9 and T10). It is attributed to the polarization mechanism that contributes to both dielectric constant and dielectric loss. According to the frequency range at which this relaxation process took place, it is likely to be caused by the space charge polarization.

The loss tangent measured from 25 to 200 °C is shown in Fig. 5. For sample T7, the lowest loss was measured at 100 °C instead of 25 °C, which may have been caused by the influence of humidity. With further increase of the temperature, loss tangent increases due to higher electrical conductivity. For sample T8 with high sintering density, the loss tangent increases gradually with the increase of temperature so that the measurement was not influenced by humidity. Decreasing loss tangent with increasing frequency indicates the dominance of conduction losses. In the case of TiO_2 samples sintered at higher temperatures, the loss peak found at room temperature still exists at high temperatures and shifts towards higher frequencies with increasing temperature. At the same time, the magnitude of the loss peak increases with increasing temperature. This observation shows that the relaxation process is thermally stimulated and the enhanced magnitude of loss peak indicates increased number of charge carriers involved in this process.

By determining the position of characteristic frequency (f_p) of the loss peak, angular frequency (ω_p, $\omega_p = 2\pi f_p$) was calculated. The temperature dependence of angular frequency was found to followed the Arrhenius law as shown in Fig. 6,

$$\omega_p = \omega_0 \exp\left(\frac{-E_a}{\kappa_B T}\right) \quad (2)$$

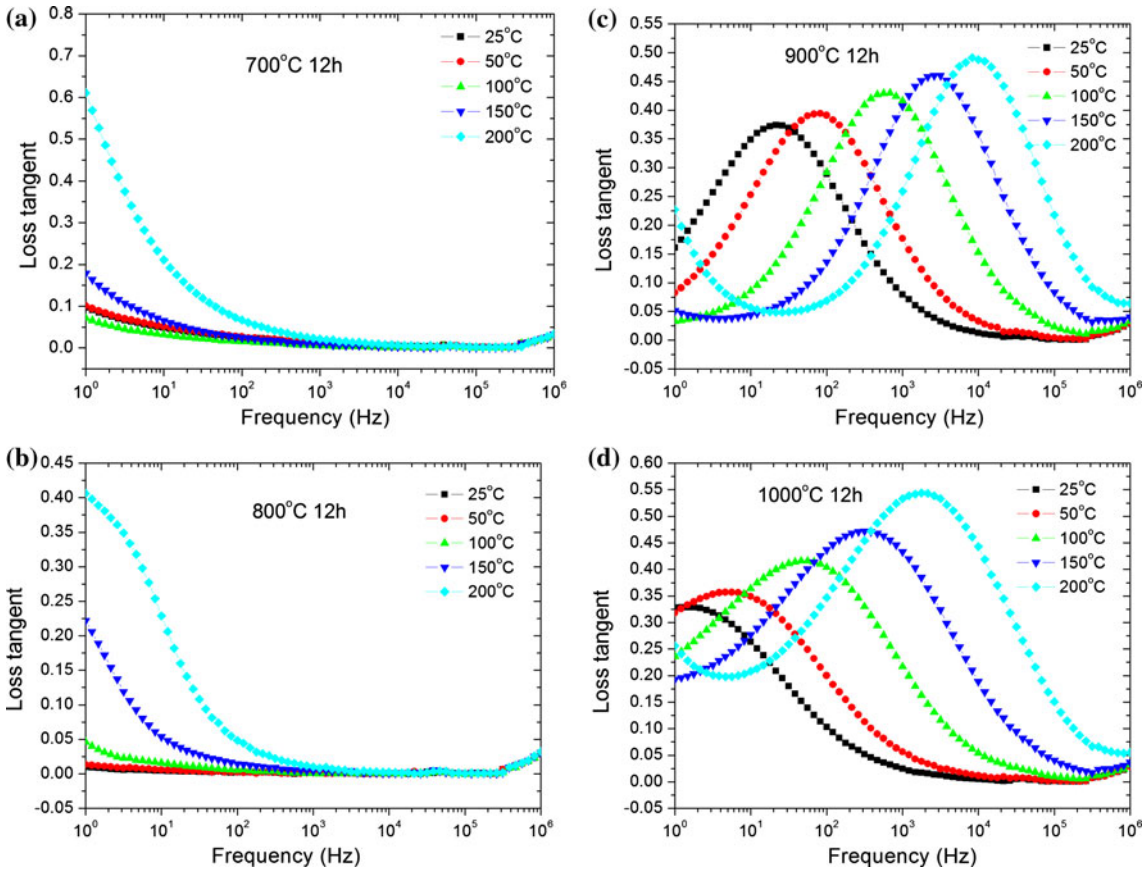

Fig. 5 Loss tangent measured from 25 °C to 200 °C for TiO_2 samples sintered at **a** 700 °C; **b** 800 °C; **c** 900 °C and **d** 1000 °C

where ω_0 is the pre-exponential factor, E_a is the activation energy and κ_B is the Boltzmann constant. Activation energies of 0.41 and 0.48 eV were obtained from sample T9 and T10, respectively. These values are close to the reported activation energy for electron hopping process [22].

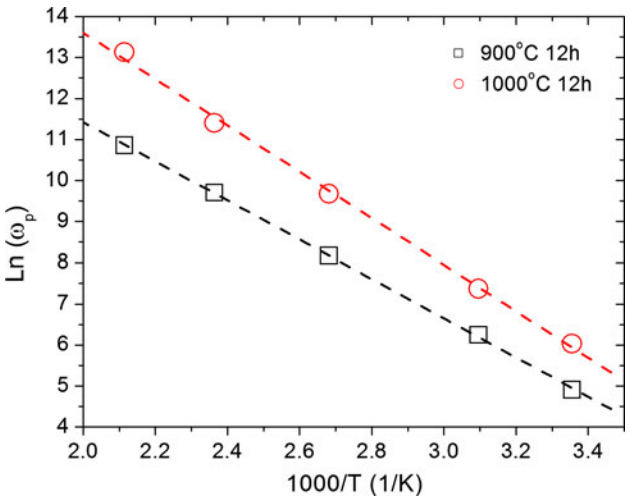

Fig. 6 Temperature dependence of loss peak angular frequency for TiO_2 ceramics sintered at 900 °C and 1000 °C

It is interesting that this relaxation process can only be found in TiO_2 sintered at high temperatures. The presence of space charge polarization indicates nonuniform resistivity within the microstructure of the samples. Since no secondary phase was identified by XRD and SEM, grain boundaries are very likely to be the region where charge pile-up takes place due to resistivity discontinuity. With the increase of sintering temperature, the grain size becomes larger whereas grain boundary density (defined as grain boundary surface area per unit volume) decreases. Therefore, TiO_2 ceramics sintered at higher temperatures with larger grain size would have higher impurity concentration at grain boundaries as aliovalent dopants/impurities tend to segregate at the grain boundaries due to the elastic strain energy and electrostatic driving force [23].

TiO_2 starting powders have ~0.1 wt% of impurity concentration, with Fe, Mg, Ca, Al as main foreign ions (Table 2). Since the ionic radius of these elements (Fe^{2+} 0.74 Å, Fe^{3+} 0.64 Å, Mg^{2+} 0.66 Å, Ca^{2+} 0.99 Å, Al^{3+} 0.51 Å) is close to the ionic radius of Ti (Ti^{4+} 0.68 Å), substitution of Ti lattice can take place. Hence, segregation of impurity ions at the grain boundaries is expected after high temperature sintering. When the impurities ions substitute the normal titanium site, point defects of M'_{Ti} or M''_{Ti}

(M represents Fe, Mg, Ca, Al) could lead to formation of negatively charged grain boundary cores generating an electron depletion layer in the nearby space charge region. In the study of Y_2O_3 doped TiO_2, due to Y segregation to the grain boundaries, negatively charge Y'_{Ti} defects gave rise to the space charge effect [24].

In order to explore this assumption, high temperature impedance spectroscopy measurements were conducted and presented as Cole–Cole plot (Fig. 7). For sample T8, a single semi-circle was obtained, while a small peak at lower frequencies was also observed. On the contrary, in case of the samples T9 and T10, their impedance responses clearly show two suppressed semi-circles. An equivalent circuit consisting of two parallel capacitor (R)—constant phase element (CPE)—connected in series can be used to represent the electrical response of the dielectric (insert in Fig. 7). The first high frequency R1-CPE1 circuit was attributed to the grain interior response, whereas the second low frequency R2-CPE2 circuit was attributed to the grain boundary response, determined by their capacitance values. It is revealed that the resistance of grain interior dominates in sample T8. With the increase of sintering temperature, contribution of grain boundaries to the total resistance of the dielectric increases. Values of grain interior resistivity (ρ_g), grain boundary resistivity (ρ_{gb}), and their relative ratio were calculated by the following equations [25]:

$$\rho_g = R_g \frac{A}{L} \tag{3}$$

$$\rho_{gb} = \frac{R_{gb}C_{gb}}{R_gC_g}\rho_g \tag{4}$$

where A is the electrode area and L is the sample thickness; C_g, C_{gb} and R_g, R_{gb} are the capacitance and resistance of grain interior and grain boundary, respectively. Table 4 shows a summary of the grain interior and grain boundary resistivity and their relative ratio. With the increase of

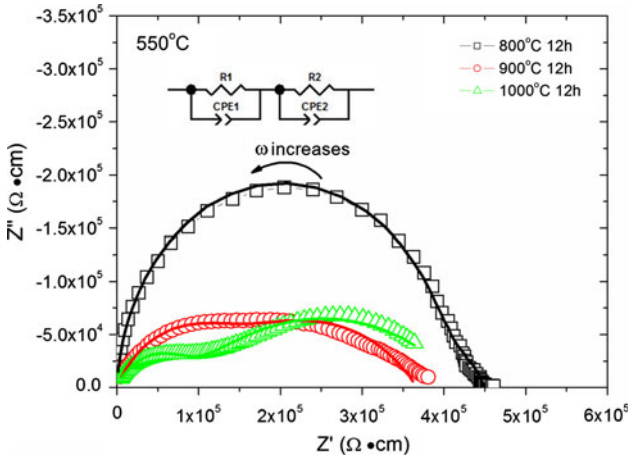

Fig. 7 Cole–Cole plot of the samples T8, T9, and T10 measured at 550 °C in air

Table 4 Fitting parameters of the impedance data measured at 550 °C

Samples	ρ_g (Ω cm)	ρ_{gb} (Ω cm)	ρ_{gb}/ρ_g	CPE1-P	CPE2-P
T8	3.96E5	9.86E6	24.9	0.97	0.73
T9	1.31E5	7.79E6	59.5	0.73	0.57
T10	8.21E4	4.35E7	530.3	0.68	0.43

sintering temperature, there is a substantial increase in the ratio of grain boundary resistivity to grain interior resistivity. Therefore, significantly enhanced resistivity difference between grain interior and grain boundary found in TiO_2 ceramics sintered at higher temperature gave rise to space charge polarization.

Constant phase element is used instead of ideal capacitor when the center of the semi-circle is depressed below the Z'-axis [24]. The magnitude of depression is a measure of the deviation from ideal capacitance behavior due to chemical or geometrical inhomogeneity [26]. From Table 4, it can be seen that the magnitude of inhomogeneity increases with the increase of sintering temperature. The semi-circle corresponding to grain boundaries was found to be more depressed than that of the grain interior, which can be attributed to a gradually changing distribution of impurity concentration among grain interiors and grain boundaries. Similar observations were made in the study of yttrium doped TiO_2 [24], so that the degree of nonuniformity in the grain boundary region increases with the increase of yttrium dopant concentration. This effect was explained by the geometric misorientation associated with grain boundaries as the misorientation parameters is to a great extent determined by the amount of excess impurity solutes at grain boundaries [27]. In the present study, since all impurities were from the starting powders, the total amount of impurities is assumed to be the same for all samples. Therefore, gradually increased nonuniformity in grain interior should be better explained by enhanced chemical inhomogeneity as original homogenously distributed impurities starts to segregate to the grain boundaries as sinter temperature increases.

In summary, it is believed that as the sintering temperature increases, more impurity ions segregated at the grain boundary region leading to greater differences in resistivity between grain interior and grain boundaries. As a result, space charge polarization occurs in TiO_2 sintered at high temperature, which accounts to a high apparent dielectric constant and loss peak.

Arrhenius plot of d.c. conductivity of TiO_2 sintered at various temperatures is shown in Fig. 8. Except for sample T7, other TiO_2 samples sintered at lower temperatures show lower conductivity. Activation energies calculated by best linear fitting for samples T7, T8, T9, and T10 are 0.79, 0.76, 0.75, and 0.76 eV, respectively (data were taken from

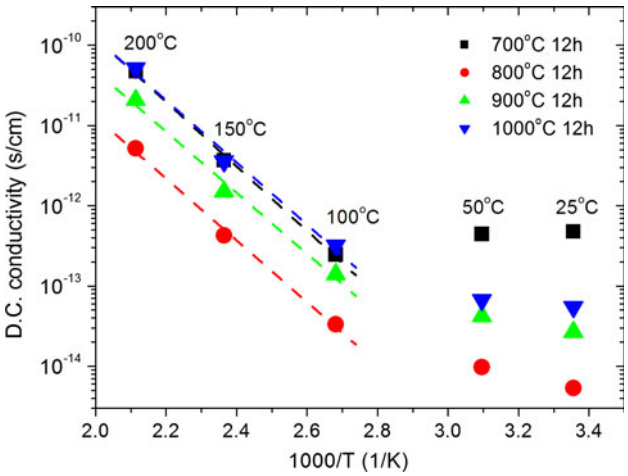

Fig. 8 Arrhenius plot of d.c. conductivity of TiO_2 samples sintered at various temperatures

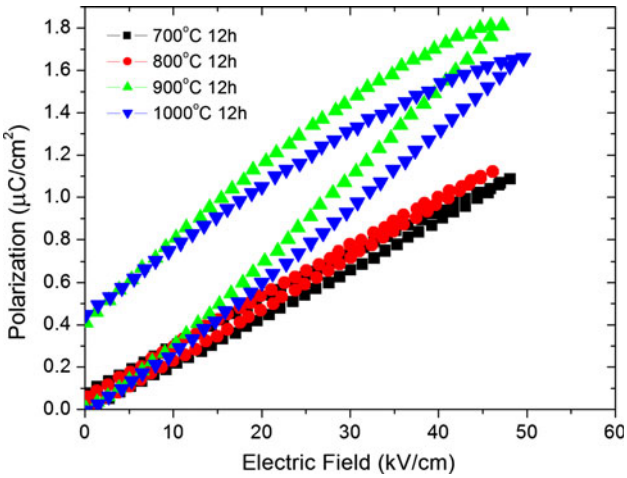

Fig. 9 Polarization versus electric field relationship of TiO_2 samples sintered at various temperatures

100 to 200 °C to exclude the influence of humidity). This activation energy is much lower than half of the band gap of TiO_2 (band gap of TiO_2: 2.90–3.33 V [28]), suggesting that in this temperature range, conductivity is controlled by defects generated during sintering at high temperatures and/or by intrinsic impurities present in the starting powders. An activation energy of ~1.23 eV was obtained in the study of TiO_2 ceramics with an average grain size ~270 nm in the temperature range from 350 to 750 °C [29]. Significantly lower activation energy observed in present study is attributed to migration of charge carriers and does not contribute to formation of new defects. Higher conductivity measured on samples sintered at higher temperatures is attributed to higher concentration of charge carriers generated at the sintering temperatures, since TiO_2 ceramics are prone to reduction at elevated temperatures [30]. This process can be described by the following defect reactions:

$$O_O^X = V_O^{\bullet\bullet} + 2e' + \frac{1}{2}O_2 \quad (5)$$

$$2O_O + Ti_{Ti} = Ti_i^{\bullet\bullet\bullet} + 3e' + O_2 \quad (6)$$

For sample T7, its particular high conductivity is due to the presence of remaining open porosity that serves as fast conduction paths [31].

The polarization–electric field (*P–E*) relationship of the samples was measured at room temperature as shown in Fig. 9. Samples T7 and T8 reveal characteristics of linear dielectrics with a linear *P–E* relation. On the contrary, *P–E* curves with a loop were obtained for samples T9 and T10. This non-linear behavior is ascribed to contribution of space charge polarization, since the crystal structure of TiO_2 does not possess permanent dipoles. Judging from the shape of *P–E* curves, sample T9 and T10 would not be desired for energy storage applications, as the encircled area in the loop represents the energy loss as heat upon discharge. The energy storage efficiency (defined as the ratio of retractable energy upon discharge to total energy stored when charging) of sample T9 and T10 are only 61.6% and 59.2%, respectively. Slim linear *P–E* curves obtained from samples T7 and T8 represent improved efficiencies with 90.6% and 92.1%, respectively. High energy storage efficiency is of critical importance because energy loss as heat increases the temperature of the dielectrics leading to higher conductivity, while enhanced conductivity in turn leads to higher loss and heat generation. Repeating of this cycle would eventually lead to thermal breakdown of the dielectric when leakage current reaches a critical level.

Dielectric breakdown strength is of prime importance in the development of dielectric materials for high energy density capacitor application. The relation between BDS and energy density is self-evident for linear dielectrics as shown in Eq. 1. More reliable BDS data can be obtained by excluding of electrical field enhancement effects at the electrode edges. However, field strength is enhanced by a significant but unknown factor at the dielectric/electrode/media triple point, leading to premature edge breakdown [16]. In this study, the problem of edge breakdown was successfully overcome by using of dimpled sample geometry. BDS data shown here were based on measurements with confirmed breakdown crater in the center of the dimple where the thinnest section of the sample is.

Room temperature BDS of the samples sintered at various temperatures is summarized in Fig. 10. Each data point is an average of six or more samples. It can be seen that with the increase of sintering temperature, BDS first increases from 640 kV/cm (T7) to a peak value of 1870 kV/cm (T8) and

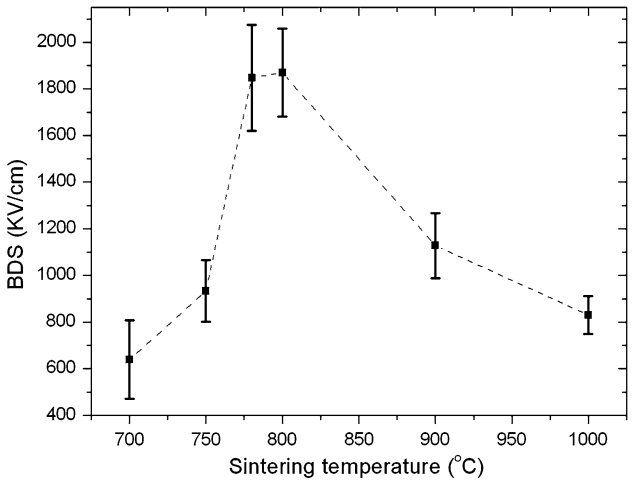

Fig. 10 Dielectric breakdown strength of TiO_2 samples as a function of sintering temperature

decreases to 831 kV/cm (T10) with further increase of the sintering temperature. This trend shows that BDS has a reverse relation with d.c. conductivity, i.e., the lower is the conductivity the higher is the BDS.

TiO_2 sintered at 700 °C has the lowest BDS mainly due to its residual porosity. Detrimental effects of porosity on the BDS of dielectric materials are well known [32]. Residual pores can intrigue partial gas discharges leading to ionization breakdown. The presence of pores in the dielectric can also lead to development of electrical field induced local stresses that can exceed externally applied electric field [33]. Beauchamp [34] found that the BDS of MgO ceramics decreased almost by a factor of three when the porosity increased to 12%.

At sintering temperature higher than 800 °C, all samples achieved a relative density over 99%. Hence, the decrease of BDS with further increase of sintering temperature cannot be attributed to the effect of porosity. Instead, it may be associated with the grain size effect. Tunkasiri and Rujijanagul [35] found a relation of BDS $\propto G^{-0.5}$ between BDS and grain size (G) in $BaTiO_3$. A similar relationship, BDS $\propto G^{-0.5}$, was found in TiO_2 dielectrics with average grain size ranging from 0.27 to 11 μm [36].

One possible explanation for higher BDS found in fine grain ceramics is the reduction of the critical flaw size. As demonstrated by Carabajar et al. [37], both mechanical strength and dielectric strength of ceramic materials were affected by critical flaw size. However, in this study, coarse grained TiO_2 has slightly higher density than that of fine grained sample, and no pores and microcracks were observed by SEM. Hence, this explanation based on critical flow size does not seem to be plausible for the present study. It was noticed that the most resistive part in coarse grained TiO_2 (T9 and T10) is the grain boundary; whereas the most resistive part in fine grained TiO_2 (T8) is the grain interior. Therefore, when an electric field is applied significant portion of the field is assumed to be held at the grain boundaries in coarse grained TiO_2, while the opposite is expected to occur in fine grained TiO_2. Since the grain boundary is a thin layer with a thickness in the range of several nanometers, a breakdown along the grain boundaries is expected at lower electrical fields. During BDS tests, a leakage current was detected before the breakdown in samples T9 and T10, that may be indicative for initiation of voltage breakdown along the grain boundary parts. Since the microstructure of the sample T8 is more uniform with a fine grain size, it is assumed that the BDS is controlled by the grain interior while breakdown along the grain boundaries is avoided. Voltage breakdown of the sample T8 always occurs before any detectable leakage current (>1 μA) can be observed.

Previously reported BDS results of TiO_2 as thin films [38] or bulk ceramics [39] are relatively low comparing with the results in this study. However, McPherson et al. [40] predicted that the BDS of TiO_2 could reach ~2500 kV/cm according to a thermochemical model. Since this model is based on invariable physical parameters of TiO_2 such as bond strength and crystal structure, this value should be considered as the intrinsic BDS of TiO_2. Our experimental results indicate that dense and nanostructured TiO_2 ceramics could possess BDS approaching to the theoretical value.

Figure 11 shows melting and crack formation at the location where breakdown occurred in sample T8. The breakdown process can be described as an explosive and sparking event, during which a sudden release of energy results in melting of the bulk material and rapid solidification. Breakdown crater with similar features were also observed in $BaTiO_3$ ceramics [35] and Al_2O_3 ceramics [41].

So far, it is not conclusive to determine the exact breakdown mechanism whether it is intrinsic (electronic), thermal, ionic, or electromechanical breakdown or a combination of them for TiO_2 ceramics studied in this work. Generally speaking, for ceramic materials the initial stage of breakdown is dominated by an electronic process whereas the later stages are controlled by thermal and electromechanical processes [41]. For sample T7 due to the residual porosity and high conductivity, ionization breakdown and or thermal breakdown mechanisms are more likely to be predominant. For sample T8, the breakdown mechanism may be electronic in nature. In case of samples T9 and T10, their breakdown events are believed to be controlled by premature breakdown of their grain boundaries as discussed in previous sections. Further studies are needed to understand the nature of the BDS with respect to

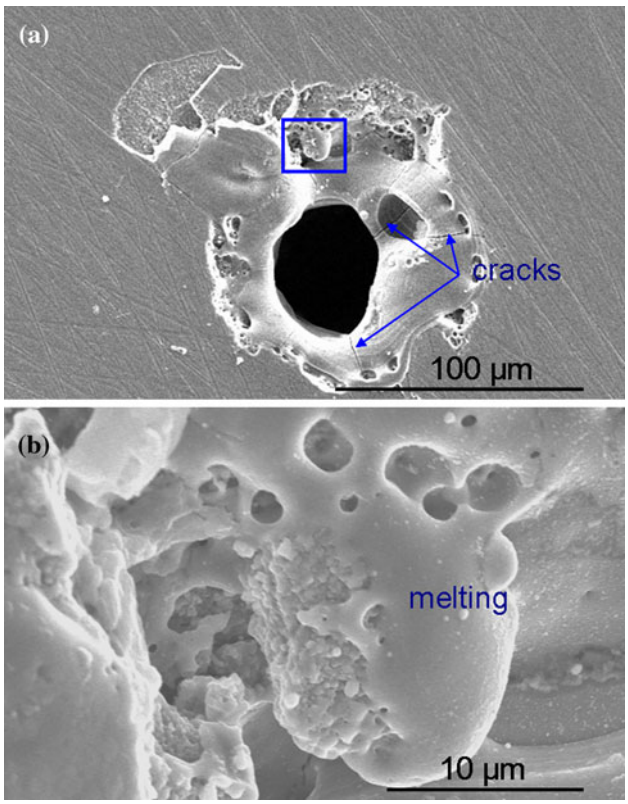

Fig. 11 **a** SEM micrographs showing a breakdown crater of a TiO_2 sample sintered at 800 °C, and **b** an enlarged view of the section indicated in **a**

the applied voltage, ramp rate, electrode materials, temperature, sample thickness, and other parameters.

Summary

Nanostructured dense TiO_2 ceramics were prepared by conventional pressureless sintering at 800 °C in oxygen atmosphere. It was found that TiO_2 ceramics with low sintering density or large grain size exhibit relatively high electrical high conductivity and dielectric loss. Space charge polarization was observed in TiO_2 ceramics sintered at high temperatures as a result of impurity segregation at grain boundaries. High BDS was achieved in TiO_2 ceramics with low conductivity and homogenous microstructure of smaller grain size. According to Eq. 6, a potential energy density ~ 15 J/cm^3 can be obtained for nanostructured TiO_2. Hence, nanostructured TiO_2 ceramics are promising dielectric materials for high energy density capacitor and pulsed power applications.

Acknowledgements The authors would like to thank Dr. Wayne Huebner and Dr. Robert Schwartz (Missouri University of Science and Technology) for their valuable suggestions. This work was supported by a MURI program sponsored by Office of Naval Research under Grant No. N000-14-05-1-0541.

References

1. Yeh YC, Tseng TT, Chang DA (1989) J Am Ceram Soc 72:1472
2. Fukushima K, Yamada I (1989) J Appl Phys 65:619
3. Regan BO, Graetzel M (1991) Nature (London) 353:737
4. Bard AJ (1980) Science 207:139
5. Ha HY, Nam SW, Lim TH, Oh IH, Hong SA (1996) J Membr Sci 111:81
6. Hoffman MR, Martin ST, Choi W, Bahenmann DW (1995) Chem Rev 95:69
7. Dervos CT, Thirios EF, Novacovich J, Vassiliou P, Skafidas P (2004) Mater Lett 58:1502
8. Ye Y, Zhang SC, Dogan F, Schamiloglu E, Gaudet J, Castro P, Roybal M, Joler M, Christodoulou C (2003) 14th IEEE Int 1:719.
9. Chen XQ, Gu GB, Liu HB, Cao ZN (2004) J Am Ceram Soc 87:1035
10. Lee KR, Kim SJ, Song JS, Lee JH, Chung YJ, Park S (2002) J Am Ceram Soc 85:341
11. Kim JH, Fujita S, Shiratori S (2006) Thin Solid Films 499:83
12. Zhou XS, Lin YH, Li B, Li LJ, Zhou JP, Nan CW (2006) J Phys D 39:558
13. Hahn H, Logas J, Averback RS (1996) J Mater Res 5:609
14. Liao SC, Colaizzi J, Chen YJ, Kear BH, Mayo WE (2000) J Am Ceram Soc 83:2163
15. Angerer P, Yu LG, Khor KA, Krumpel G (2004) Mater Sci Eng A 381:16
16. Yoshimura M, Bowen HK (1981) J Am Ceram Soc 64:404
17. Chao S, Petrovsky V, Dogan F (2006) Proceeding of advanced dielectric materials and electronic devices, materials science and technology (MS&T) 2006: materials and systems, vol 1, p 707
18. Lee YI, Lee JH, Hong SH, Kim DY (2003) Mater Res Bull 38:925
19. Campbell IE, Sherwood EM (eds) (1967) High-temperature materials and technology. Wiley, New York
20. Eastman JA (1994) J Appl Phys 75:770
21. Tobar ME, Krupka J, Ivanov EN, Woode RA (1998) J Appl Phys 83:1604
22. Tuller HL, Nowick AS (1977) J Phys Chem Solids 38:859
23. Yan MF, Cannon RM, Bowen HK (1983) J Appl Phys 54:764
24. Wang QL, Varghese O, Grimes CA, Dickey EC (2007) Solid State Ion 178:187
25. Guo X, Maier J (2001) J Electrochem Soc 148:E121
26. Macdonald JR (1987) Impedance spectroscopy: emphasizing solid materials and systems. Wiley, New York
27. Wynblatt P, Rohrer GS, Papillon F (2003) J Eur Ceram Soc 23:2841
28. Bak T, Nowotny J, Rekas M, Sorrell CC (2003) J Phys Chem Solids 64:1043
29. Hoshino K, Peterson NL, Wiley CL (1985) J Phys Chem Solids 46:1397
30. Pullar RC, Penn SJ, Wang XR, Reaney IM, Alford NM (2009) J Eur Ceram Soc 29:419
31. Song SH, Wang X, Xiao P (2002) Mater Sci Eng B 94:40
32. Morse CT, Hill GJ (1970) Proc Br Ceram Soc 18:23
33. Young AL, Hilmas GE, Zhang SC, Schwartz RW (2007) J Mater Sci 42:5613. doi:10.1007/s10853-006-1116-2
34. Beauchamp EK (1971) J Am Ceram Soc 54:484
35. Tunkasiri T, Rujijanagul G (1996) J Mater Sci Lett 15:1767
36. Yang Y (2003) Master Thesis, University of Missouri-Rolla
37. Carabajar S, Olagnon C, Fantozzi G, Gressus CL (1995) IEEE Annu Rep 11:278
38. Souni ME, Oja I, Krunks M (2004) J Mater Sci Mater Electron 15:341
39. Kishimoto A, Koumoto K, Yanagida H (1989) J Am Ceram Soc 72:1373
40. McPherson J, Kim JY, Shanware A, Mogul H (2003) Appl Phys Lett 82:2121
41. Owate IO, Freer R (1992) J Appl Phys 72:2418